JOURNAL OF GEOPHYSICAL RESEARCH, VOL. 112, B07404, doi:10.1029/2006JB004738, 2007

Nondestructive continuous physical property measurements of core samples recovered from hole B, Taiwan Chelungpu-Fault Drilling Project

Tetsuro Hirono,[1,2] En-Chao Yeh,[3] Weiren Lin,[2] Hiroki Sone,[4] Toshiaki Mishima,[5] Wonn Soh,[2] Yoshitaka Hashimoto,[6] Osamu Matsubayashi,[7] Kan Aoike,[8] Hisao Ito,[8] Masataka Kinoshita,[9] Masafumi Murayama,[5] Sheng-Rong Song,[3] Kuo-Fong Ma,[10] Jih-Hao Hung,[10] Chien-Ying Wang,[10] Yi-Ben Tsai,[10] Tomomi Kondo,[11] Masahiro Nishimura,[11] Soichi Moriya,[11] Tomoyuki Tanaka,[11] Toru Fujiki,[11] Lena Maeda,[11] Hiroaki Muraki,[11] Toshikatsu Kuramoto,[11] Kazuhiro Sugiyama,[11] and Toshikatsu Sugawara[11]

Received 6 September 2006; revised 14 March 2007; accepted 5 April 2007; published 7 July 2007.

[1] The Taiwan Chelungpu-Fault Drilling Project was undertaken in 2002 to investigate the faulting mechanism of the 1999 M_w 7.6 Taiwan Chi-Chi earthquake. Hole B penetrated the Chelungpu fault, and core samples were recovered from between 948.42- and 1352.60-m depth. Three major zones, designated FZB1136 (fault zone at 1136-m depth in hole B), FZB1194, and FZB1243, were recognized in the core samples as active fault zones within the Chelungpu fault. Nondestructive continuous physical property measurements, conducted on all core samples, revealed that the three major fault zones were characterized by low gamma ray attenuation (GRA) densities and high magnetic susceptibilities. Extensive fracturing and cracks within the fault zones and/or loss of atoms with high atomic number, but not a measurement artifact, might have caused the low GRA densities, whereas the high magnetic susceptibility values might have resulted from the formation of magnetic minerals from paramagnetic minerals by frictional heating. Minor fault zones were characterized by low GRA densities and no change in magnetic susceptibility, and the latter may indicate that these minor zones experienced relatively low frictional heating. Magnetic susceptibility in a fault zone may be key to the determination that frictional heating occurred during an earthquake on the fault.

Citation: Hirono, T., et al. (2007), Nondestructive continuous physical property measurements of core samples recovered from hole B, Taiwan Chelungpu-Fault Drilling Project, *J. Geophys. Res.*, *112*, B07404, doi:10.1029/2006JB004738.

1. Introduction

[2] The 21 September 1999 Chi-Chi, Taiwan earthquake (M_w7.6) was the largest inland earthquake recorded in Taiwan in the twentieth century. The hypocenter was located at 23.853°N and 120.816°E with a focal depth of 8 km [*Ma et al.*, 1999] (Figure 1). The earthquake initiated from the hypocenter in southern Chelungpu fault and ruptured both updip and laterally northward [*Chen et al.*, 2001; *Kikuchi et al.*, 2000; *Ma et al.*, 2000]. The faulting produced surface ruptures about 100 km long along the Chelungpu fault with largest net slip of up to 11.5 m in the north [*Lee et al.*, 2003]. The motion was of thrust type with a left-lateral component, and the fault is one of the western deep thrust in the Taiwan mountain belt (Figure 1).

[3] The Chi-Chi earthquake was well recorded by a dense seismic observatory network (Taiwan Strong Motion Network) operated by the Central Weather Bureau [*Shin et al.*, 2000]. The stations near the northern end of the Chelungpu fault recorded the largest ground velocities and

[1]Department of Earth and Space Science, Graduate School of Science, Osaka University, Toyonaka, Osaka, Japan.
[2]Kochi Institute for Core Sample Research, Japan Agency for Marine-Earth Science and Technology, Nankoku, Kochi, Japan.
[3]Department of Geosciences, National Taiwan University, Taipei, Taiwan.
[4]Department of Geophysics, School of Earth Sciences, Stanford University, Stanford, California, USA.
[5]Center for Advanced Marine Core Research, Kochi University, Nankoku, Kochi, Japan.

0148-0227/07/2006JB004738$09.00

[6]Department of Natural Environmental Science, Faculty of Science, Kochi University, Kochi, Japan.
[7]Institute for Geo-Resources and Environment, National Institute of Advanced Industrial Science and Technology, Tsukuba, Japan.
[8]Center for Deep Earth Exploration, Japan Agency for Marine-Earth Science and Technology, Yokohama, Japan.
[9]Institute for Research on Earth Evolution, Japan Agency for Marine-Earth Science and Technology, Yokosuka, Japan.
[10]Institute of Geophysics, National Central University, Jhongli, Taiwan.
[11]Marine Works Japan Ltd., Yokohama, Japan.

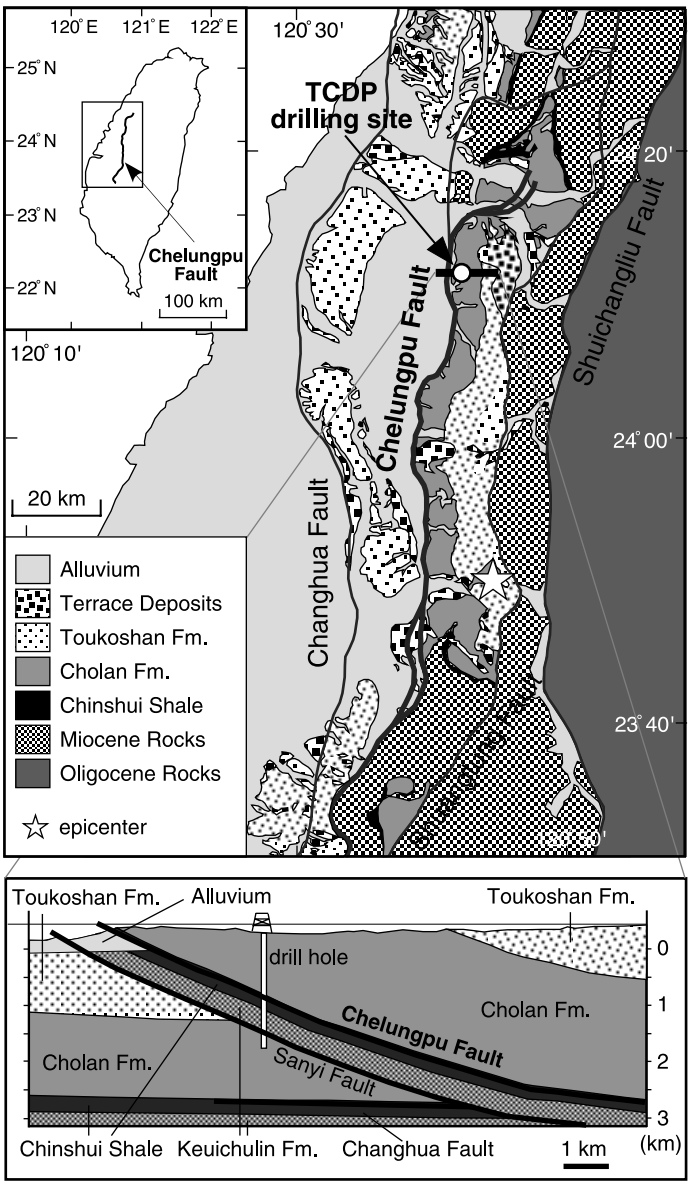

Figure 1. Geological map of central Taiwan, modified from the work of *Wang et al.* [2000], with the site of the Taiwan Chelungpu-fault Drilling Project (TCDP) and an E-W cross section through the site location.

displacements, up to 3 m/s and 8 m, respectively [*Chung and Shin*, 1999]. In contrast, ground accelerations were higher in the southern part of the fault, even though the ground velocities and fault displacements were less there than in the north. *Andrews* [2005] proposed that differences in the effect of thermal pressurization, combined with the differences in the lithology of units within the fault zones in the north and south, explained these contrasting slips. Another notable contrast in slip behaviors was the marked absence of high-frequency radiation recorded in the near-field seismograms at the northern part of the fault. *Ma et al.* [2003] attributed this absence to the slip mechanism, elasto-hydrodynamic lubrication [*Brodsky and Kanamori*, 2001], by assuming the presence of viscous fluidized fault gouge within the fault zone. They suggested that the increased lubrication pressure widened the gap between the fault surfaces, thereby reducing the areas of asperity in contact and decreasing high-frequency radiation.

[4] However, thermal pressurization and hydrodynamic lubrication are merely hypothesized at present and need to be investigated further through observation and analysis of rock samples. To further investigate the faulting mechanism of the Chi-Chi earthquake, the Taiwan Chelungpu-Fault Drilling Project (TCDP) was started in 2002. TCDP drilled two cored holes, hole A (total depth 2003.00 m) and hole B (total depth 1352.60 m). In hole B, cores were recovered only from between 948.42 and 1352.60 m, and the core samples were sent to the Kochi Institute for Core Sample Research, Japan Agency for Marine-Earth Science and Technology (JAMSTEC), for nondestructive continuous physical property measurements. These measurements provide basic information to assist in the characterization of

lithologic units and the correlation of cored material with downhole logging data, thus contributing to our understanding of the nature of the faulting at the 1999 Chi-Chi earthquake.

[5] Although preliminary density, magnetic susceptibility, and natural gamma ray measurement results, only within the fault zones, were reported by *Hirono et al.* [2006b], complete lithological descriptions, as well as other measurement results, for all core samples from hole B have not yet been reported. In this paper, we report the results of density, porosity, magnetic susceptibility, and natural gamma ray measurements for all core samples and present those from within the Chelungpu fault in detail. We also describe the fault zone architectures and discuss the faulting mechanism of the 1999 Chi-Chi earthquake.

2. Drilling Procedure and Core Sample Handling

[6] TCDP drilled to 1352.60-m depth in hole B (40 m northwest of hole A) but recovered core samples only from between 948.42 and 1352.60 m. The borehole drilling was conducted by the JV team of Fengyeu Drilling Co., Ltd. and Wanda Technical Consultants Corp. There were four casings within hole B before the coring (0–12 m, 20 in. × 9.52 mm, ASTM A53B casing; 0–50 m, 14 in. × 9.52 mm, ASTM A53B casing; 0–400 m, 9-5/8 in. × 10 mm, API N-80 40 casing; 0–945 m, 7 in. × 10 mm, API N-80 casing). Wireline coring was conducted between 948.42 and 1352.60 m with a PQ (83-mm diameter) core barrel. The drilling mud was circulated at around 1.1 g/cm^3 during coring, and the core recovery rate reached nearly 100%. Core samples were recovered completely even within the damaged fault zones.

[7] Immediately after retrieval, the core samples were packaged into aluminum tube cases at the drilling site to prevent evaporation of the fluids within the core samples. Atmospheric air trapped within the case was replaced with nitrogen gas before sealing to prevent any oxidization. Then the core samples were placed in a refrigerated container and shipped to Kochi Institute, JAMSTEC, for nondestructive continuous physical property measurements. We confirmed at Kochi that the samples were received in good condition without any collapsed, dried, or oxidized parts.

3. Nondestructive Continuous Physical Property Measurements

[8] A flowchart of the core sample measurement process at the Kochi Institute is shown in Figure 2. First, an X-ray computerized tomography (CT) image was captured while the core sample was still sealed within the aluminum case. Next, after the core sample had equilibrated with room temperature, approximately 25°C, the density, magnetic susceptibility, and natural gamma radiation were measured using a Multi-Sensor Core Logger (MSCL) system (Geotek Ltd., London, UK) on whole-round core sections. Then the whole-round core samples were split into archive and working half cores with a large rock cutter. Water content and thermal conductivity were measured on the archive half-core samples, which were also used for the geological description. In addition, a photo image capture logger, color spectroscopy, and an X-ray Fluorescence Spectroscopy core logger were used to collect data and images of the split surfaces. The porosity and density were measured on discrete subsamples collected from the working half-core samples.

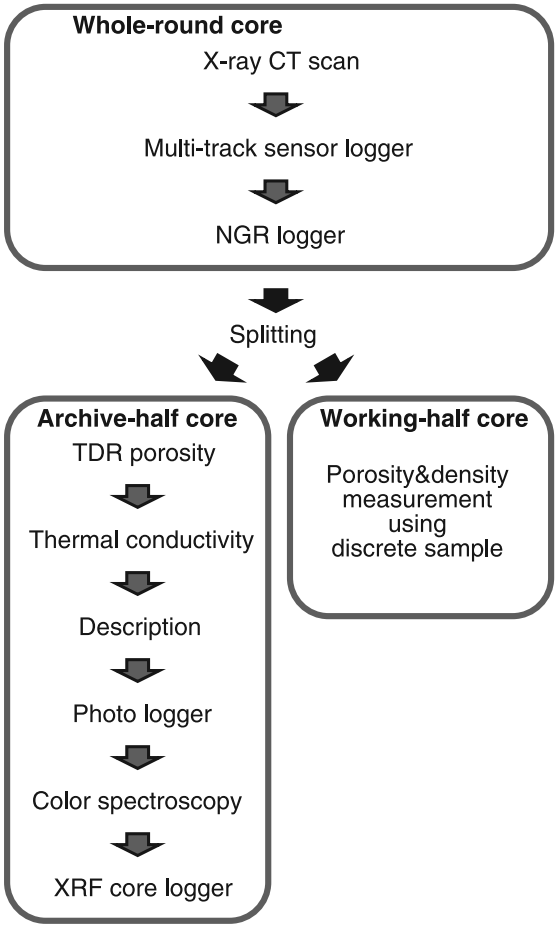

Figure 2. Flow chart of nondestructive continuous physical property measurement on the core samples recovered from hole B, TCDP.

[9] In this paper, we report only X-ray CT image, density (both MSCL and discrete sample), magnetic susceptibility, natural gamma ray radiation, and porosity data. The methods are further described below.

3.1. X-Ray CT Image

[10] The method of X-ray CT is a radiological imaging technique in which attenuation of two-dimensional X-ray fan beams that penetrate a sample is measured by an array of detectors. A two-dimensional image of the distribution of linear X-ray attenuation is reconstructed by Radon transform and Fourier projection-slice theorem. A three-dimensional data set of the sample is then obtained by stacking continuous two-dimensional images. The degree of X-ray attenuation depends on both the density and the atomic number of the material composing the samples. Higher density and higher atomic numbers result in higher attenuation of X-rays.

[11] An X-ray CT scanner (Pratico, Hitachi Medical Co.) was here used not for three-dimensional imaging of core samples but for the two-dimensional imaging. X-rays were

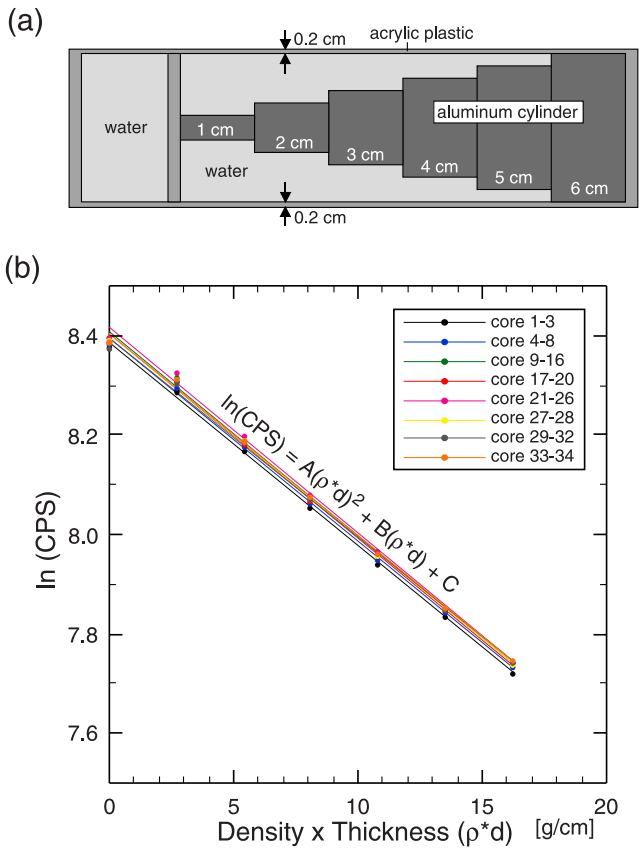

Figure 3. Calibration for GRA density. (a) Schematic diagram of calibration cylinders. (b) Relationship between ρd and ln I.

produced by bombarding a molybdenum-tungsten alloy target with electrons in an X-ray tube at 120 kV and 100 mA, and the transmitted X-rays through core samples were captured by four-arrayed detectors. Brighter colors in the processed image mean higher attenuation of X-rays. The resolution of each image was 1 mm/pixel.

[12] The X-ray CT images, produced by X-rays having varying energy levels, are subject to noise, which results from sample size, the random manner in which the photons are distributed within the image, and varying electron current and acceleration conditions [*Hirono et al.*, 2003]. Thus the results reported of analyses based on the X-ray CT images in this study are only semiquantitative.

3.2. Gamma Ray Attenuation (GRA) Density

[13] A thin gamma ray beam was provided by a 137-Cs gamma ray source at a radiation level of 370 Bq within a lead shield with a 2.5-mm collimator. The gamma ray detector comprised a scintillator and an integral photomultiplier tube. The calculation of bulk density from gamma ray attenuation was by the following equation:

$$\rho = 1/(\mu d) \times \ln(I_0/I), \tag{1}$$

where ρ is sediment bulk density, μ is the Compton attenuation coefficient, d is sample thickness, I_0 is the gamma source intensity, and I is the measured intensity through the sample. Because μ and I_0 are treated as constants, ρ can be calculated from I. We used a set of aligned aluminum cylinders of various thicknesses, surrounded by distilled water in a sealed acrylic container, for calibration (Figure 3a). Gamma counts were taken through each cylinder for long count time (60 s), and ln I was plotted against ρd (Figure 3b). Here ρ of each aluminum cylinder was 2.7 g/cm^3, and d was 1, 2, 3, 4, 5, or 6 cm. The relationship between I and ρd can be expressed as follows:

$$\ln I = A(\rho * d)^2 + B(\rho * d) + C, \tag{2}$$

where A, B, and C are coefficients determined during calibration. These coefficients fluctuated slightly during the measurements. The values resulting from each calibration test are summarized in Table 1.

[14] The MSCL provided the values of I and d, and ρ was calculated with the above-described equation. This density measurement was conducted every 0.5 cm for 4 s. The spatial resolution was 5 mm, so each data point reflects the properties of the closest 5-mm interval. Accuracy is discussed later, in comparison with the densities measured on discrete samples.

3.3. Magnetic Susceptibility

[15] Magnetic susceptibility is the degree to which a material can be magnetized by an external magnetic field. A Bartington loop sensor (MS2C) with a 10-cm loop diameter was used for magnetic susceptibility measurements. An oscillator circuit in the sensor produces a low-intensity (approximately 80 A/m RMS) nonsaturating, alternating magnetic field (0.565 kHz). Any material near the sensor that has a magnetic susceptibility causes a change in the oscillator frequency. This pulse frequency is then converted into magnetic susceptibility values.

[16] The magnetic susceptibility values obtained were volume-specific and were corrected for the relative effect of core size and the size of the loop sensor being used. The spatial resolution of the loop sensor was 20–30 mm, and it was accurate to within less than 2%. Like the GRA density data, magnetic susceptibility data were obtained at 0.5-cm intervals with a 4-s acquisition time. The integration time period was 1.0 s.

3.4. Natural Gamma Radiation (NGR)

[17] Natural gamma ray emissions were recorded from all core sections to determine variations in the radioactive counts of the samples and for a correlation with the downhole NGR measurements. A lead-shielded counter was used, which was optically coupled to a photomultiplier tube and connected to a bias base that supplied the high-voltage power and a signal preamplifier. Two sensors were mounted horizontally in a lead cube-shaped housing. The NGR system records radioactive decay of ^{40}K, ^{232}Th, and ^{238}U, which are three long-period isotopes that decay at an essentially constant rate within measurable timescales. The spatial resolution was 150 mm, and NGR was measured every 10 cm over a 2-min period. For fault-related core samples only, it was measured every 2 cm over the same period. Background radiation noise was 38 cps, measured by inserting a blank filled with quartz powder, and the accuracy of the measured data was within about 1.5%.

Table 1. Values of the coefficients, A, B, and C, in $\ln I = A(\rho d)^2 + B(\rho d) + C$

	$\ln(\mathrm{CPS}) = A(\rho * d)^2 + B(\rho * d) + C$		
Core	A	B	C
1–3	−0.0002	−0.0595	8.8473
4–8	−0.0002	−0.0595	8.8538
9–16	−0.0003	−0.0587	8.8665
17–20	−0.000001	−0.0648	8.8956
21–26	−0.0005	−0.054	8.8459
27, 28	−0.0004	−0.0556	8.8426
29–32	−0.0005	−0.0500	8.7975
33, 34	−0.0004	−0.0551	8.8387
35–50	−0.0001	−0.0605	8.8573
51–66	−0.0002	−0.0581	8.8398
67–80	−0.0001	−0.0611	8.8599
81–94	−0.0002	−0.0584	8.8506
95–110	−0.0002	−0.0591	8.8412
111–117	−0.00003	−0.0635	8.8394
118–132	−0.0003	−0.0577	8.8451
133–138	−0.0004	−0.0533	8.8023
139–150	−0.0002	−0.0579	8.8360
151–158	−0.0004	−0.0542	8.8192
159–170	−0.0002	−0.0577	8.8458
171–184	−0.00003	−0.0628	8.8724
185–198	−0.0002	−0.0579	8.8422
199, 200	−0.0002	−0.0584	8.8506
201–203	−0.0014	−0.0246	8.6166
202, 204	−0.0000001	−0.0645	8.8989
205–214	−0.000003	−0.0652	8.9024
215–223	−0.0002	−0.0592	8.8642
224–232	−0.0003	−0.0532	8.8083
233–238	−0.0003	−0.0555	8.8366
239–243	−0.0003	−0.0556	8.8341
244–249	−0.0001	−0.0674	8.9078
250–255	−0.0009	−0.0379	8.7021
256–264	−0.0006	−0.0477	8.7731
265–268	−0.00001	−0.0649	8.8949
269–276	−0.0008	−0.0414	8.7228
277–284	−0.000004	−0.0637	8.8805
285–290	−0.0011	−0.0316	8.6538
291–297	−0.0013	−0.0261	8.6108
298–306	−0.0001	−0.0609	8.8501
307–314	−0.0006	−0.0477	8.7571
315, 316	−0.00001	−0.0649	8.8949
317–322	−0.0010	−0.0362	8.6886
323–328	−0.0002	−0.0600	8.8460
329–335	−0.0004	−0.0544	8.8304
336–337	−0.0008	−0.0431	8.7305
338–348	−0.0003	−0.0551	8.8291
349–356	−0.0005	−0.0501	8.7896
357–366	−0.0002	−0.0577	8.8383
367–370	−0.0004	−0.0542	8.8192
371, 372	−0.0001	−0.0611	8.8599
373–390	−0.0001	−0.0668	8.8872
391–396	−0.0007	−0.0454	8.7561
397–406	−0.0001	−0.0620	8.8551
407–420	−0.0005	−0.0519	8.7672
421–431	−0.0009	−0.0418	8.7526

3.5. Porosity and Density

[18] Porosity and density of discrete subsamples from the working half-core samples were measured. One rock subsample was collected from each 1-m-long core sample. Because each subsample was fully water saturated, the wet mass, M_{wet}, was first measured with a precision of ±0.001 g on an electronic balance. Then the subsample was oven-dried at 105 ± 5°C for 24 hours and allowed to cool in a desiccator, and the dry mass, M_{dry}, and volume, V_{dry}, were measured. The dry volume was determined at least three times with a helium-displacement pycnometer (Quantachrome Penta-Pycnometer) with a nominal precision of ±0.01 cm^3 and then averaged. Pore volume, V_{pore}, was calculated by subtracting dry mass from wet mass, assuming a constant 1.0 $\mathrm{g/cm}^3$ density for the pore fluid evaporated during drying. Then porosity and wet-bulk density were calculated as:

$$\mathrm{Porosity} = \left\{ V_{\mathrm{pore}} / \left(V_{\mathrm{pore}} + V_{\mathrm{dry}} \right) \right\} \times 100 \tag{3}$$

$$\mathrm{Wet\ bulk\ density} = M_{\mathrm{wet}} / \left(V_{\mathrm{pore}} + V_{\mathrm{dry}} \right) \tag{4}$$

Porosity and density were accurate to within 0.1 and 0.01 $\mathrm{g/cm}^3$, respectively.

3.6. Correlation Between GRA Density and Discrete Sample Density

[19] The correlation between density determined from the GRA and that measured on discrete samples was determined for each lithology (Figure 4). Five typical lithologies were recognized in the core samples: sandstone; siltstone; interbedded sandstone and siltstone (majority sandstone); interbedded sandstone and siltstone (majority siltstone); and fault-related rock (fault gouge and breccia). Because the wet bulk density data calculated on discrete samples had high accuracy, within 0.01 $\mathrm{g/cm}^3$, they were used as standards. For all the lithologies, the GRA densities were generally approximately 0.1 $\mathrm{g/cm}^3$ higher than those measured on the discrete samples. This difference was inferred to result from variation in chemical composition within the core samples. The amount of attenuation of gamma rays depends not only on density but also on the chemical composition of the material. Aluminum cylinders were used to calibrate the GRA density measurements, but material composed of atoms with higher atomic numbers than aluminum would cause higher attenuation. Because natural rocks such as the sandstone and siltstone of these TCDP core samples include atoms with atomic numbers higher than that of Al (for example, Si, K, Ca, Fe), the GRA density measurements of natural rocks based on the calibration with aluminum would result in higher apparent densities than those measured on discrete samples.

4. Characteristics of All Core Samples

4.1. Lithology

[20] Stratigraphically, the depth interval from 948.42 to 1040 m corresponds to the Pliocene to Pleistocene Cholan Formation, which is composed dominantly of sandstone and sandstone-siltstone alternation with weak to heavy bioturbation. The Pliocene Chinshui Shale occurs from 1040- to 1280-m depth and consists predominantly of siltstone with weak bioturbation. From 1280- to 1352.60-m depth is the late Miocene to early Pliocene Kueichulin Formation, which is composed dominantly of massive sandstone with minor siltstone.

[21] *Wang et al.* [2000, 2002] and *Yue et al.* [2005] suggested that the Chelungpu fault was a bedding-parallel thrust in the Chinshui Shale. We found, consistent with their interpretation, three dominant fault zones as the Chelungpu fault system within the Chinshui Shale. These zones are at

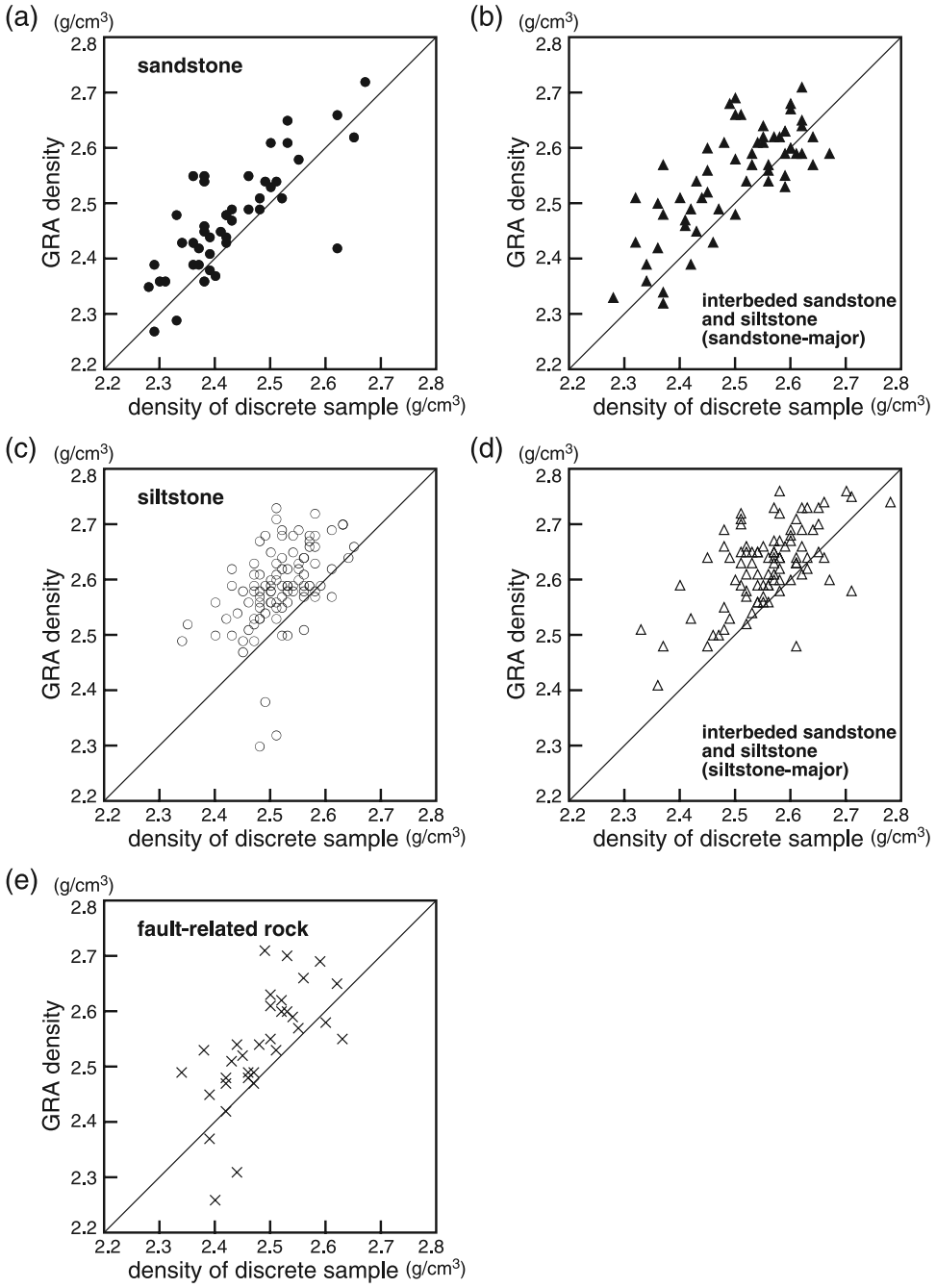

Figure 4. Cross plots of GRA density and density on discrete samples. (a) Sandstone, (b) majority sandstone interbedded sandstone and siltstone, (c) siltstone, (d) majority siltstone interbedded sandstone and siltstone, (e) fault-related rock.

depths of 1134–1137, 1194–1197, and 1242–1244 m and were previously called 1136mFZ, 1194mFZ, and 1243mFZ, respectively [*Hirono et al.*, 2006b]. We have renamed them here as FZB1136, FZB1194, and FZB1243, respectively. Structural descriptions are presented in section 5. Three major fault zones, FZA1111, FZA1153, and FZA1222, were also found within the Chinshui Shale in hole A [*Yeh et al.*, 2007; *Sone et al.*, 2007]. The correlation of these zones between holes A and B is discussed later. Although the major fault zones are parallel or subparallel to the bedding planes, the fault zones can be easily distinguished from the shale layers because they are accompanied by fault zone architecture such as fault gouge and breccia.

4.2. Physical Properties

[22] GRA density, magnetic susceptibility, and NGR values, and porosity and density values measured on discrete samples, for all core samples in hole B are summarized in Figure 5.

[23] In the Cholan Formation (948.42–1037 m), the GRA densities ranged approximately from 2.3 to 2.8 g/cm^3,

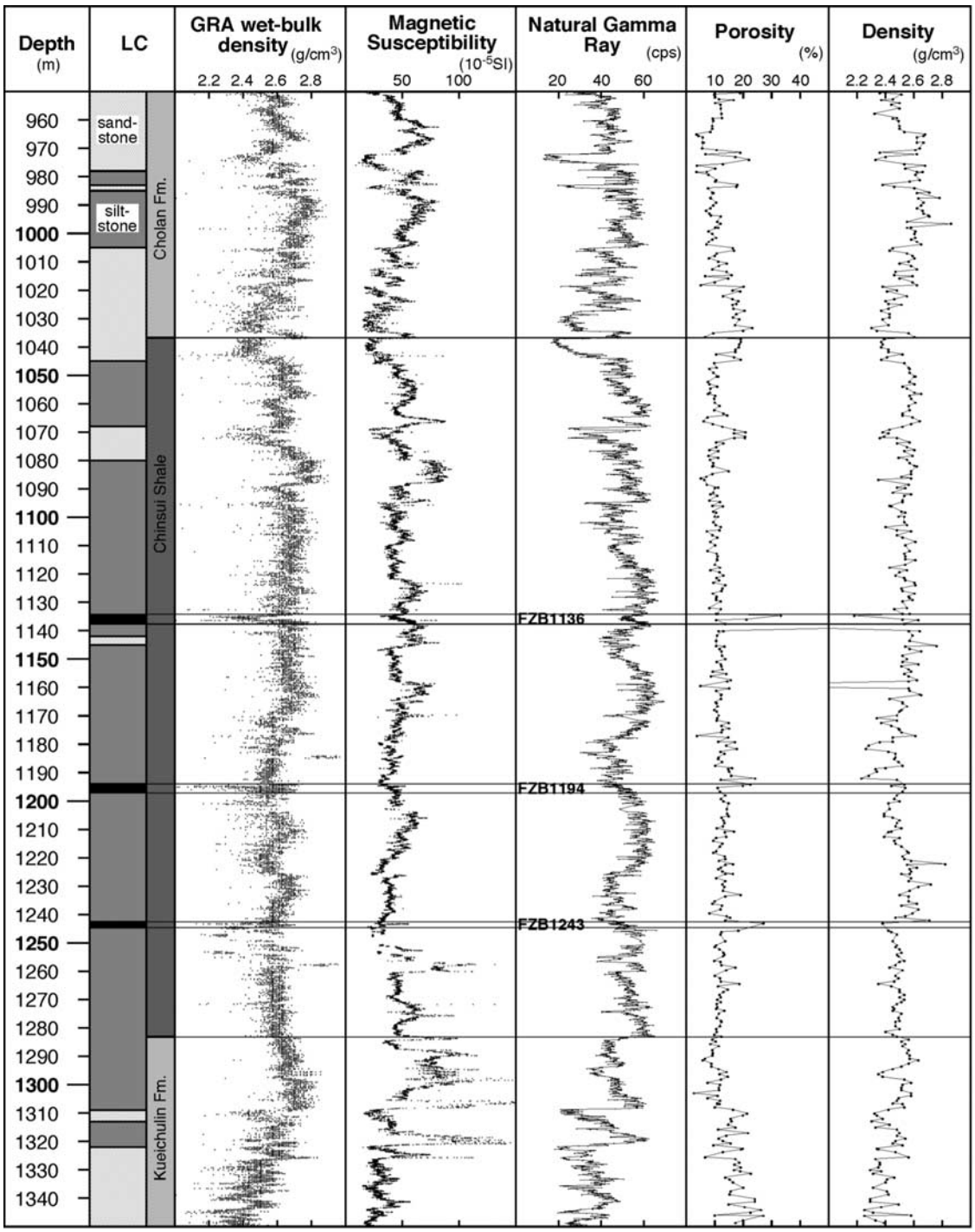

Figure 5. GRA density, magnetic susceptibility, natural gamma ray radiation, porosity, and density by discrete sample logs from hole B. LC, lithological column.

magnetic susceptibilities from 20×10^{-5} to 80×10^{-5} SI, NGR emissions from 10 to 60 cps, porosities from 5 to 20%, and densities of discrete samples from 2.3 to 2.7 g/cm^3. Both GRA densities and discrete sample densities were relatively higher in the siltstone layers than in the sandstone layers.

[24] In the Chinshui Shale (1037–1283 m), except in the three fault zones (the data are presented later), the GRA densities were approximately constant at 2.6 g/cm^3, magnetic susceptibilities ranged from 30×10^{-5} to 150×10^{-5} SI, NGR emissions from 40 to 60 cps, porosities from 5 to 20%, and densities measured on discrete samples from 2.3 to 2.7 g/cm^3. A slight correlation between the GRA densities and magnetic susceptibilities was recognized, and rhythmic fluctuations from high to low were observed in the NGR emissions. Relatively high NGR emissions were associated with pure siltstone and majority siltstone interbedded between sandstone and siltstone.

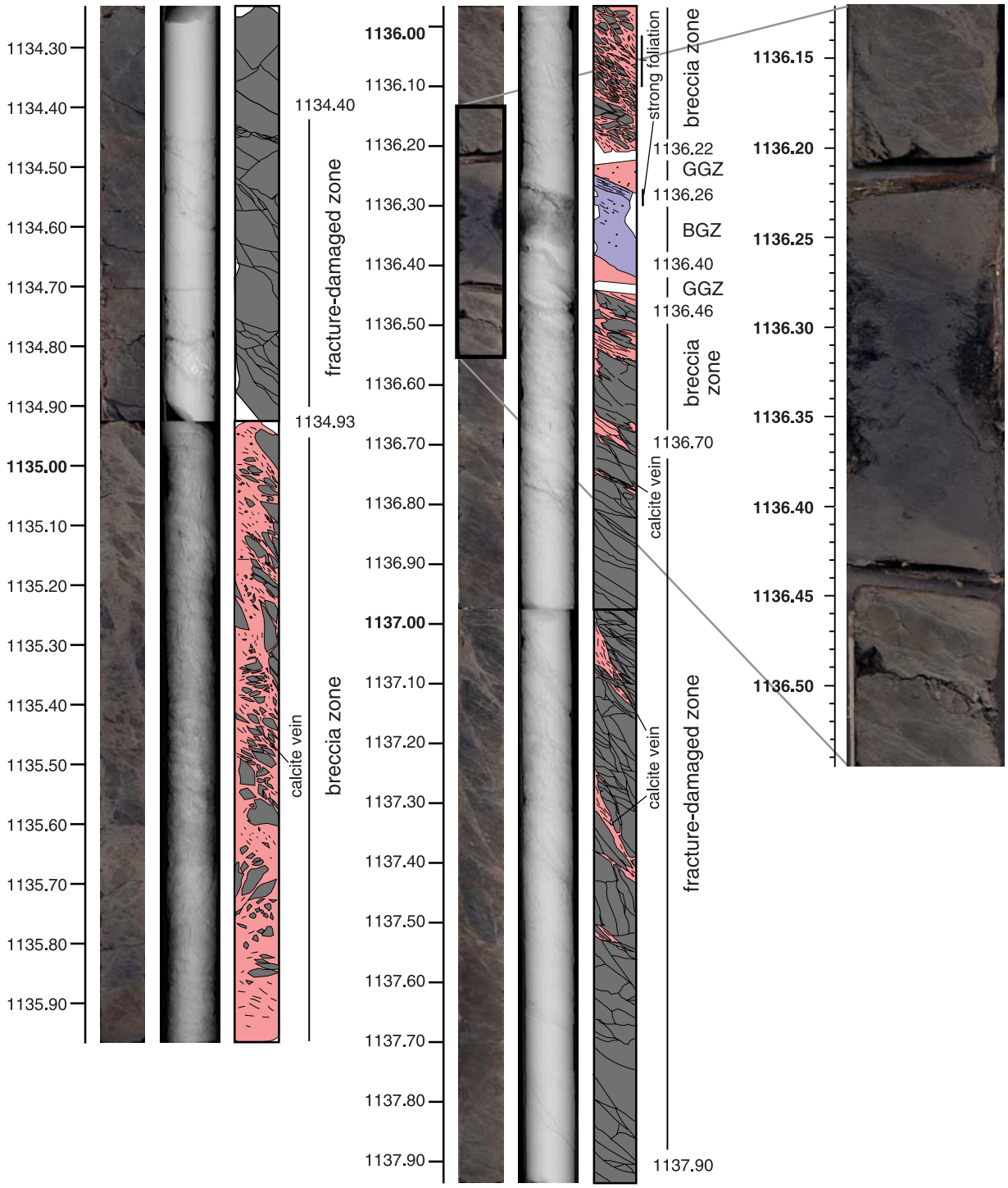

Figure 6. Fault zone architecture of FZB1136. Photos, X-ray CT images, and sketches are shown from left to right. BGZ, black gouge zone; GGZ, gray gouge zone.

[25] In the Kueichulin Formation (1283–1352.60 m), the GRA densities ranged approximately from 2.1 to 2.6 g/cm^3, magnetic susceptibilities from 20×10^{-5} to 200×10^{-5} SI, NGR emissions from 20 to 60 cps, porosities from 5 to 30%, and densities of discrete samples from 2.2 to 2.6 g/cm^3. Relatively low GRA densities and magnetic susceptibilities were associated with pure sandstone and majority sandstone interbedded between sandstone and siltstone.

[26] At all depths, regions of high magnetic susceptibility generally coincided with regions of high GRA density. A possible explanation is that rocks with higher density contain more magnetic minerals, under the assumption of a constant volumetric fraction of the minerals. Regions of high NGR emission also generally coincided with those of high GRA density. The cause may be similar in that the rocks

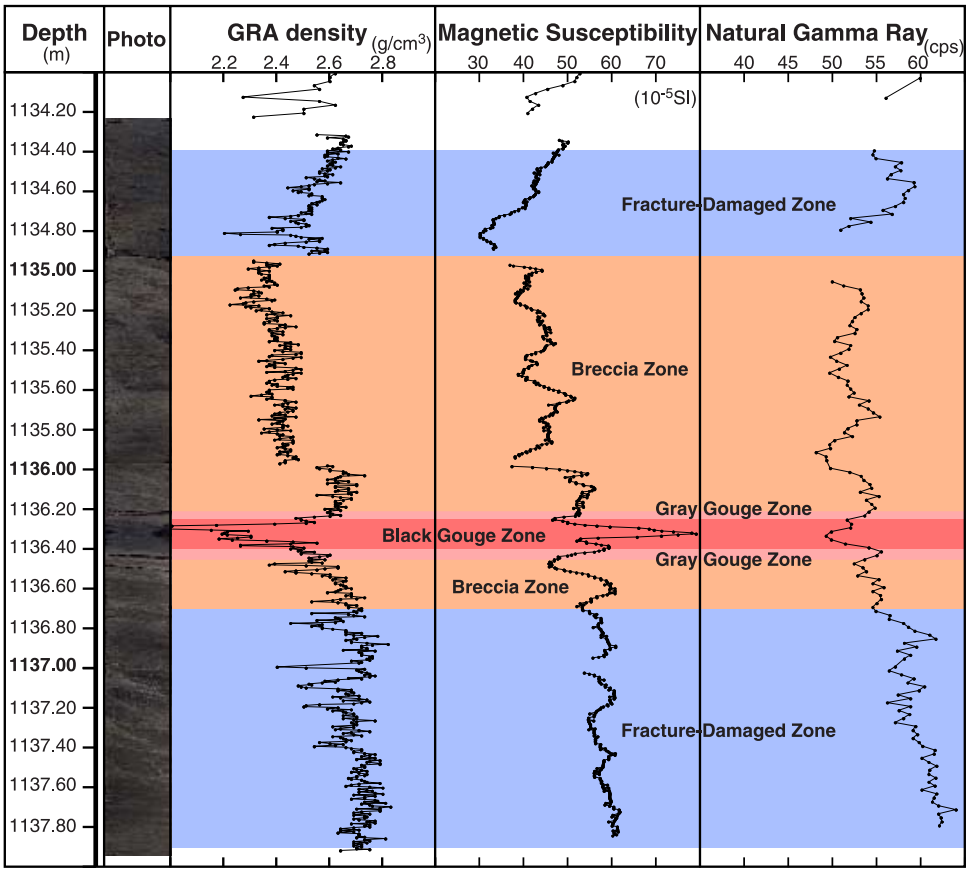

Figure 7. Density, magnetic susceptibility, and natural gamma ray radiation (NGR) logs from FZB1136.

with higher density contain more minerals, such as clay minerals, containing K, Th, and U.

5. Characteristics of the Three Major Fault Zones

5.1. FZB1136: Fault Zone Structures

[27] The fault rocks were classified into fracture-damaged zone, fault breccia (breccia zone), and fault gouge, following the terminology of *Sibson* [1977], *Chester et al.* [1993], *Schulz and Evans* [1998], and *Biegel and Sammis* [2004]. In FZB1136, the following subzones were encountered, from top to bottom (Figure 6): upper fracture-damaged zone (1134.40–1134.93 m), upper breccia zone (1134.93–1136.22 m), upper gray fault gouge (1136.22–1136.26 m), black fault gouge (1136.26–1136.40 m), lower gray fault gouge (1136.40–1136.46 m), lower breccia zone (1136.46–1136.70 m), and lower fracture-damaged zone (1136.70–1137.90 m). Both fracture-damaged zones displayed layer-parallel and layer-subparallel open fractures, which gradually increased in frequency toward the breccia and fault gouge zones, but were sparse except in the vicinity of the fault zones, within the alternation of sandstone and mudstone with bioturbation. In both breccia zones, the clasts were composed of very fine-grained sandstone or siltstone with minor shear bands, and the foliations within the matrixes became more intense closer to the gouge zones. Both gouge zones displayed foliation or random fabric textures, usually with a gradual transition from one zone to another. The dip angles of distinct shear planes within gouge zones were approximately 35°.

5.2. FZB1136: Physical Properties

[28] The GRA density, magnetic susceptibility, and NGR data obtained from FZB1136 are summarized in Figure 7. The GRA densities ranged from 2.4 to 2.7 g/cm^3 but were significantly lower within the black gouge zone (approximately 2.0–2.4 g/cm^3). Lower X-ray attenuation on the X-ray CT image of the zone is consistent with the lower densities (Figure 6). Densities recorded in the upper breccia zone were lower relative to those in other zones, except that in the black gouge zone. Magnetic susceptibilities fluctuated mainly from 30×10^{-5} to 60×10^{-5} SI but also showed higher peak values within the black gouge zone (approximately $50–80 \times 10^{-5}$ SI). The NGR emissions ranged from 48 to 68 cps and did not show a strong relationship to the architecture of the fault zone. Across the fault zone, magnetic susceptibilities increased with depth, and the NGR emissions appeared to increase in the footwalls.

[29] High magnetic susceptibility and high NGR emission generally accompanied high GRA density because, as we explained in section 4.2, rocks with higher density can contain more magnetic and radioactive minerals; however, in the black gouge zone, lower GRA density was associated with higher magnetic susceptibility.

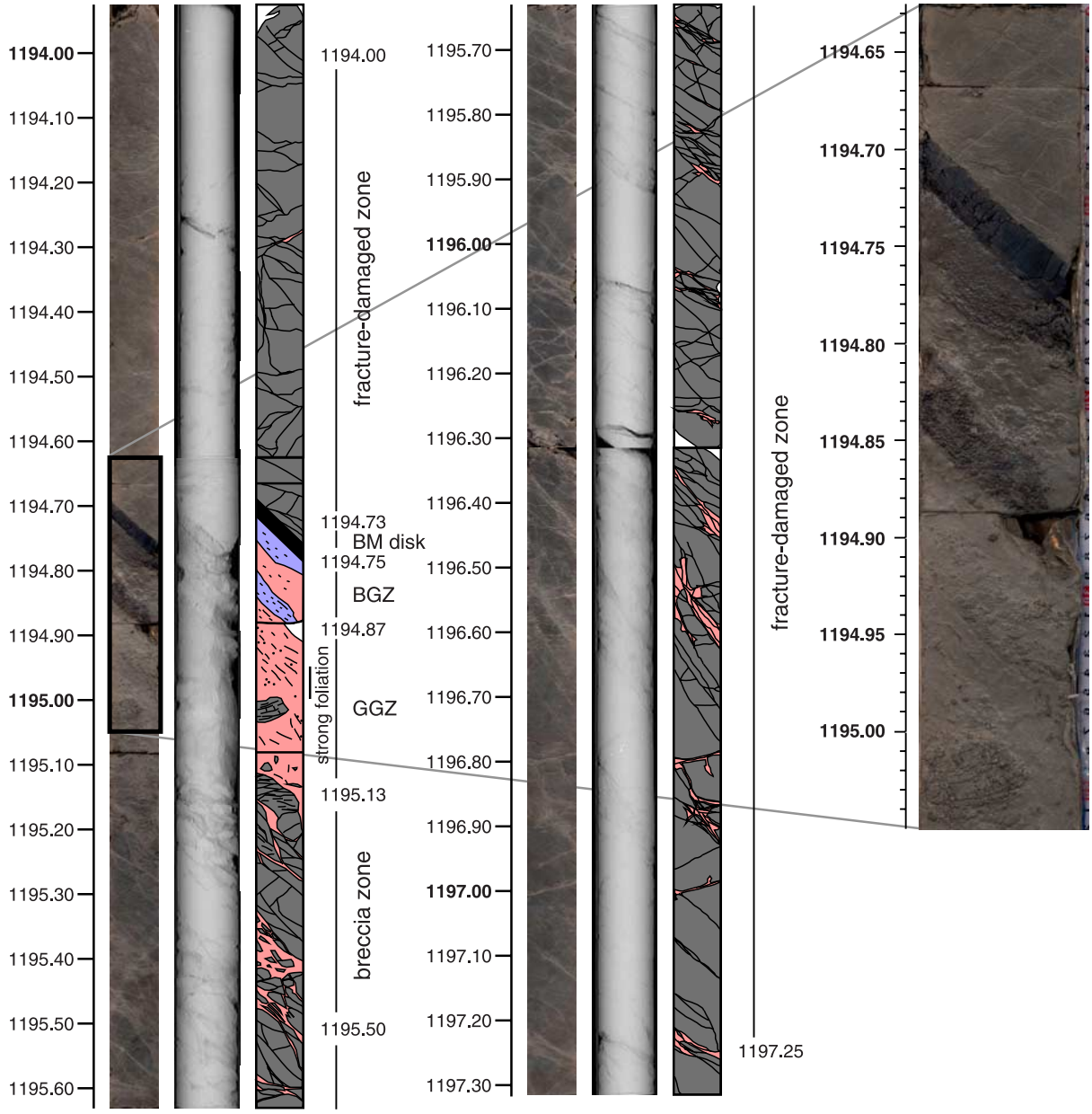

Figure 8. Fault zone architecture of FZB1194. The images are photo, X-ray CT, and sketch from left to right. BM disk; disk-shaped black material; BGZ, black gouge zone; GGZ, gray gouge zone.

5.3. FZB1194: Fault Zone Structures

[30] In FZB1194, subdivisions observed from top to bottom were (Figure 8) upper fracture-damaged zone (1194.00–1194.73 m), black fault gouge (1194.73–1194.87 m), gray fault gouge (1194.87–1195.13 m), breccia zone (1195.13–1195.50 m), and lower fracture-damaged zone (1195.50–1197.25 m). The upper sandstone unit included minor shear bands. The black fault gouge included disk-shaped black material (1194.73–1194.75 m), referred to as the BM disk [*Hirono et al.*, 2006b], which has been identified as pseudotachylyte by a low degree of melting [*Hirono et al.*, 2006a]. It was 2 cm thick and relatively stiff compared to the gouge. The dip angle of this disk was approximately 45°. The upper boundary between the BM disk and the adjacent upper cohesive sandstone unit was extremely sharp, whereas fragments of the disk were contained in the underlying black gouge. Other parts of both gouge zones displayed foliation or random fabric texture. The breccia zone in FZB1194 was thinner than that in FZB1136, less foliation seemed to have developed within the zone itself, and the clasts were mainly fine-grained sandstone. The fracture-damaged zones displayed similar characteristics to those of FZB1136.

5.4. FZB1194: Physical Properties

[31] The GRA density, magnetic susceptibility, and NGR data obtained from FZB1194 are summarized in Figure 9. The GRA densities ranged approximately from 2.0 to 2.7 g/cm^3 and magnetic susceptibilities from 28 $\times$ 10^{-5} to 52 $\times$ 10^{-5} SI. In the black gouge zone, lower GRA densities (approximately 2.2–2.4 g/cm^3) and higher

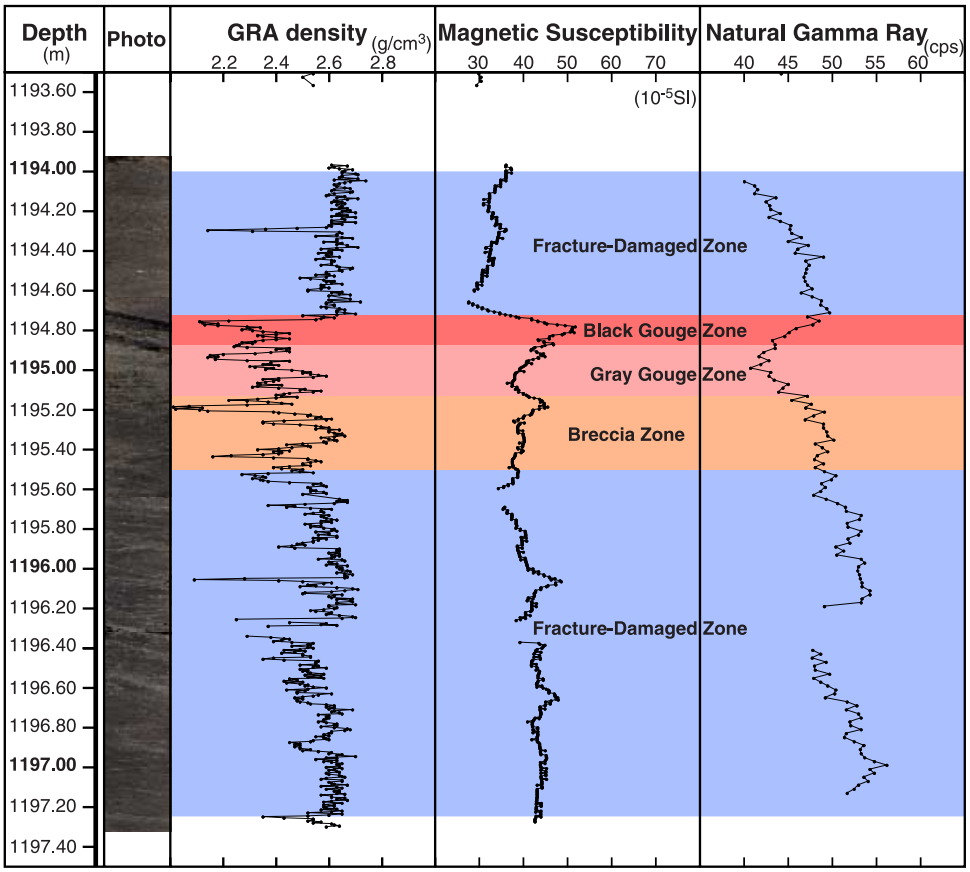

Figure 9. Density, magnetic susceptibility, and natural gamma ray radiation (NGR) logs from FZB1194.

magnetic susceptibilities (approximately 50 $\times$ 10^{-5} SI) were recognized. Lower X-ray attenuation on the X-ray CT image of the zone is consistent with the lower densities (Figure 8). NGR emissions ranged from 40 to 57 cps and showed lower values around the gray gouge zone. Across the fault zone, the NGR emissions appeared to increase in the footwall.

5.5. FZB1243: Fault Zone Structures

[32] In FZB1243, subdivisions observed from top to bottom were (Figure 10) upper fracture-damaged zone (1242.70–1243.33 m), upper gray fault gouge (1243.33–1243.38 m), black fault gouge (1243.38–1243.50 m), lower gray fault gouge (1243.50–1243.60 m), and lower fracture-damaged zone (1143.60–1244.30 m). The black fault gouge included disk-shaped black material (1243.38–1243.41 m), referred to as the BM disk [*Hirono et al.*, 2006b], which has been identified as pseudotachylyte by a low degree of melting [*Hirono et al.*, 2006a]. It was 3 cm thick, and relatively stiff compared to the gouge, similar to that encountered in FZB1194. The dip angle of this disk was approximately 30°. Other parts of both gouge zones displayed foliation or random fabric texture. The fracture-damaged zones displayed similar characteristics to those in the other two fault zones. The overall scale of FZB1243 was smaller compared with the shallower two fault zones, as no breccia zone was present between the intact rocks and the fault gouge zones and the fault rocks were confined within a region approximately 25 cm thick.

5.6. FZB1243: Physical Properties

[33] The GRA density, magnetic susceptibility, and NGR data obtained from FZB1243 are summarized in Figure 11. The GRA densities ranged approximately from 2.1 to 2.7 g/cm^3 and magnetic susceptibilities from 27 $\times$ 10^{-5} to 54 $\times$ 10^{-5} SI. In the black gouge zone, lower GRA densities (approximately 2.2–2.5 g/cm^3) and higher magnetic susceptibilities (approximately 40–55 $\times$ 10^{-5} SI) were recognized. Lower X-ray attenuation on the X-ray CT image of the zone is consistent with the lower densities (Figure 10). NGR emissions ranged from 43 to 57 cps, and the lower values show good correlation with the black gouge zone. Across the fault zone, the NGR emissions appeared to increase in the footwalls.

5.7. Correlation of Major Fault Zones Between in Holes A and B

[34] The three major fault zones in hole A, reported by *Yeh et al.* [2007] and *Sone et al.* [2007], FZA1111 (fault zone at 1111-m depth in hole A), FZA1153, and FZA1222, may correspond to FZB1136, FZB1194, and FZB1243, respectively, on the basis of the relative depth deviation calculated from the horizontal distance between the holes (40 m), the angle and direction of dip of the fault zones, and observation of host rock lithology. The spatial relation-

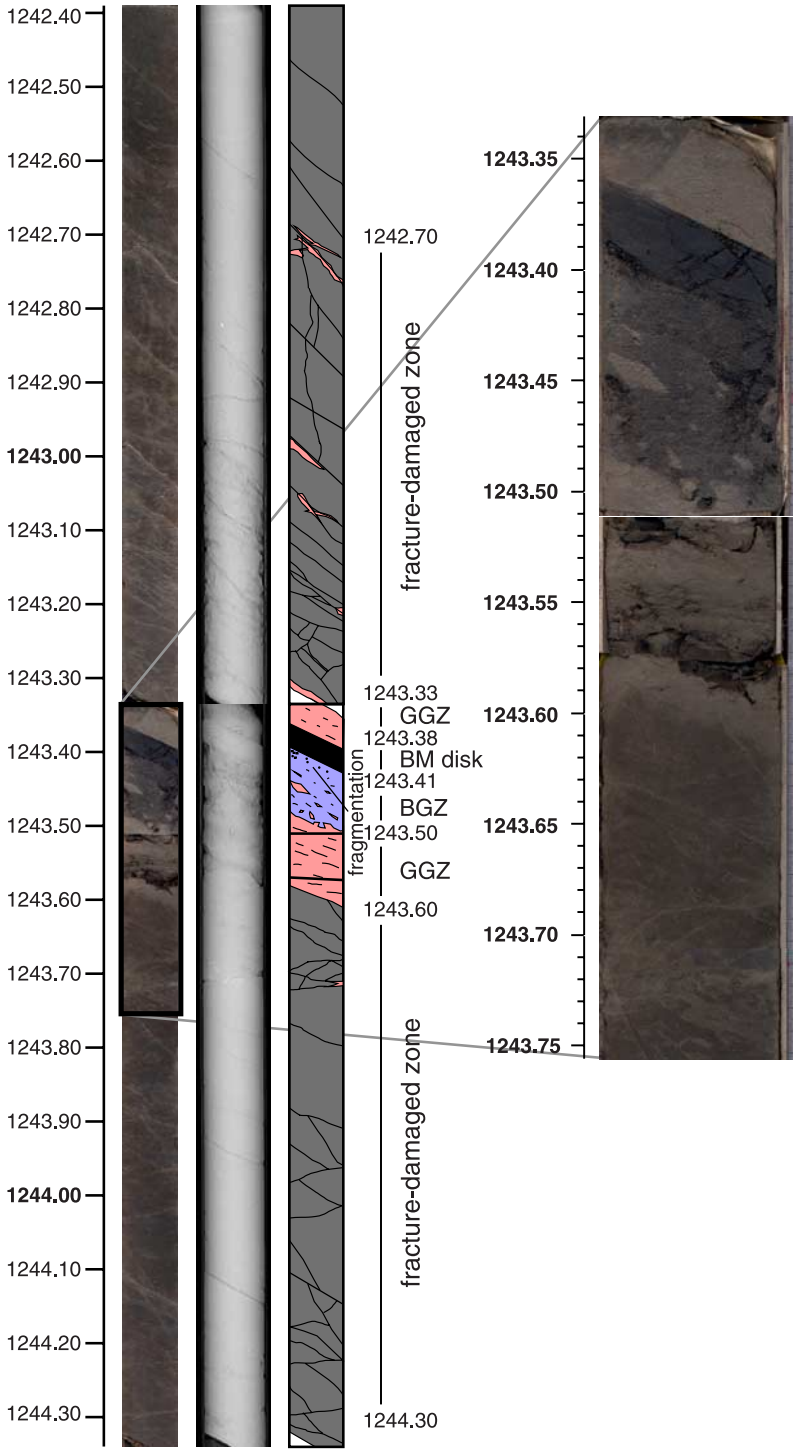

Figure 10. Fault zone architecture of FZB1243. The images are photo, X-ray CT, and sketch from left to right. BM disk; disk-shaped black material; BGZ, black gouge zone; GGZ, gray gouge zone.

ships of the fault zones between the two holes are illustrated in Figure 12.

6. Characteristics of the Minor Fault Zones

[35] In hole B, there were many minor fault zones throughout the core samples. Representative minor fault zones were observed at depths of around 1067.49, 1067.80, 1314.27, 1317.84, and 1340.94 m. The physical property measurements results are shown alongside the photo images (Figure 13).

[36] Fault breccia, with 2-cm thickness, was developed within the minor fault zone at 1067.49 m. Fragmentation was recognized around the boundaries with the upper and lower host rocks. The GRA density was lower at 2.36 g/cm^3 than that of the host rock, whereas the magnetic susceptibility did not change (Figure 13a).

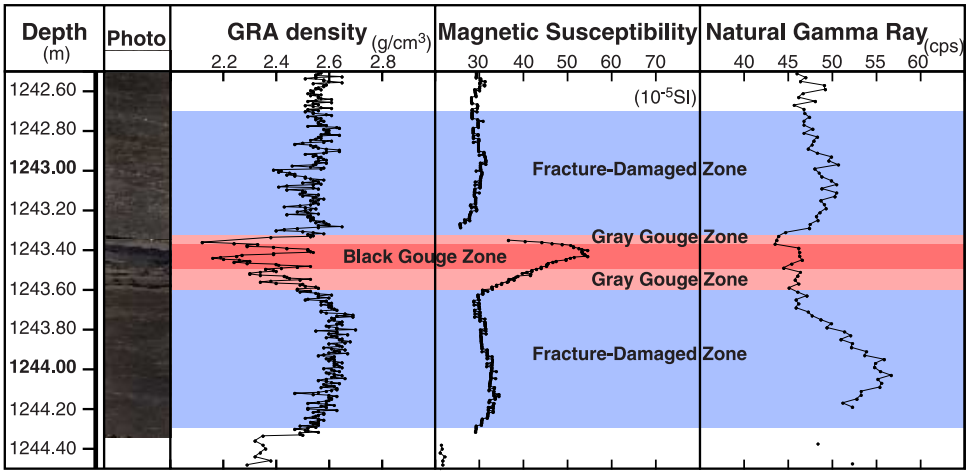

Figure 11. Density, magnetic susceptibility, and natural gamma ray radiation (NGR) logs from FZB1243.

[37] Within the minor fault zone at 1067.80 m, fault breccia and gouge, with a total thickness of 6 cm, were observed. Fragmentation was recognized around the boundaries with the upper and lower host rocks. The GRA density was also lower, 2.34 g/cm^3, than that of the host rock, whereas the magnetic susceptibility did not change (Figure 13a).

[38] Black fault gouge, 1 cm in thickness, was observed within the minor fault zone at 1314.27 m. The boundaries with the upper and lower host rocks were sharp. The fault gouge had slightly lower GRA density, 2.53 g/cm^3, than the host rock, and no change of magnetic susceptibility was observed (Figure 13b).

[39] Fault gouge, 2 cm in thickness, was observed within the minor fault zone at 1317.84 m. The boundary with the upper host rock was gradual, whereas that with the lower host rock was sharp. The gouge had a significantly lower GRA density, 2.16 g/cm^3, and lower magnetic susceptibility, 45×10^{-5} SI, than the host rock (Figure 13c). However, the part with minimum susceptibility, 36×10^{-5} SI, was observed 4 cm below the gouge. In the lower host rock, the magnetic susceptibility fluctuated, perhaps in relation to the lithology.

[40] The minor fault zone at 1340.94 m was thicker than the others (total thickness, 20 cm). An upper breccia zone, a black gouge zone, and a lower breccia zone were observed. The GRA densities were lower, with a minimum value of 2.21 g/cm^3, than those of the host rocks, whereas the magnetic susceptibility did not change (Figure 13d).

[41] Within these minor fault zones, the interval of measurement of NGR emissions (10 cm) did not result in measurements with high enough resolution to detect a signal from the fault zones themselves, but the parts including the fault zones did not show any change compared with the other parts. It is thus likely that no specific fluctuations occurred within the minor fault zones.

[42] Therefore the minor fault zones are characterized by lower GRA density and no change in magnetic susceptibility or NGR emission.

7. Discussion

7.1. Low GRA Density Within All Fault Zones

[43] In all three major fault zones (FZB1136, FZB1194, and FZB1243), relatively lower GRA densities were recorded within each black gouge zone. Similarly, lower GRA densities were also observed within all minor fault zones.

[44] First, it is possible that these lower GRA densities represent a measurement artifact. Sample from the gouge

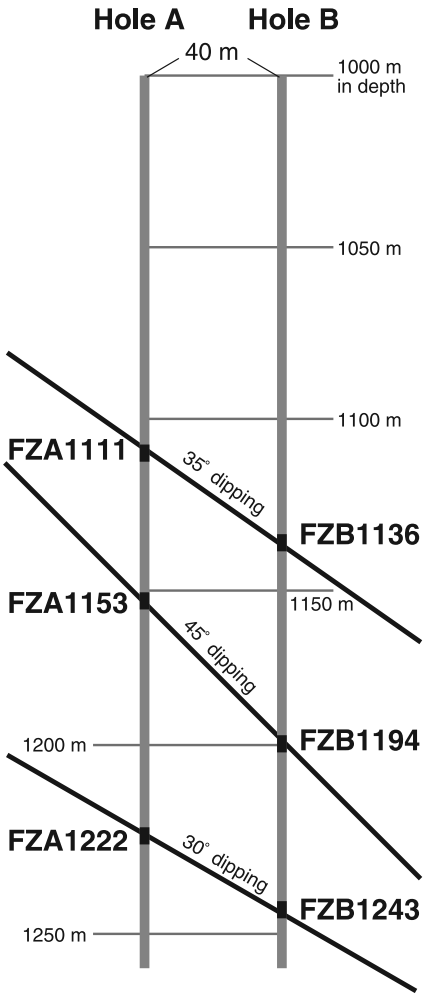

Figure 12. Correlations of major three fault zones between holes A and B.

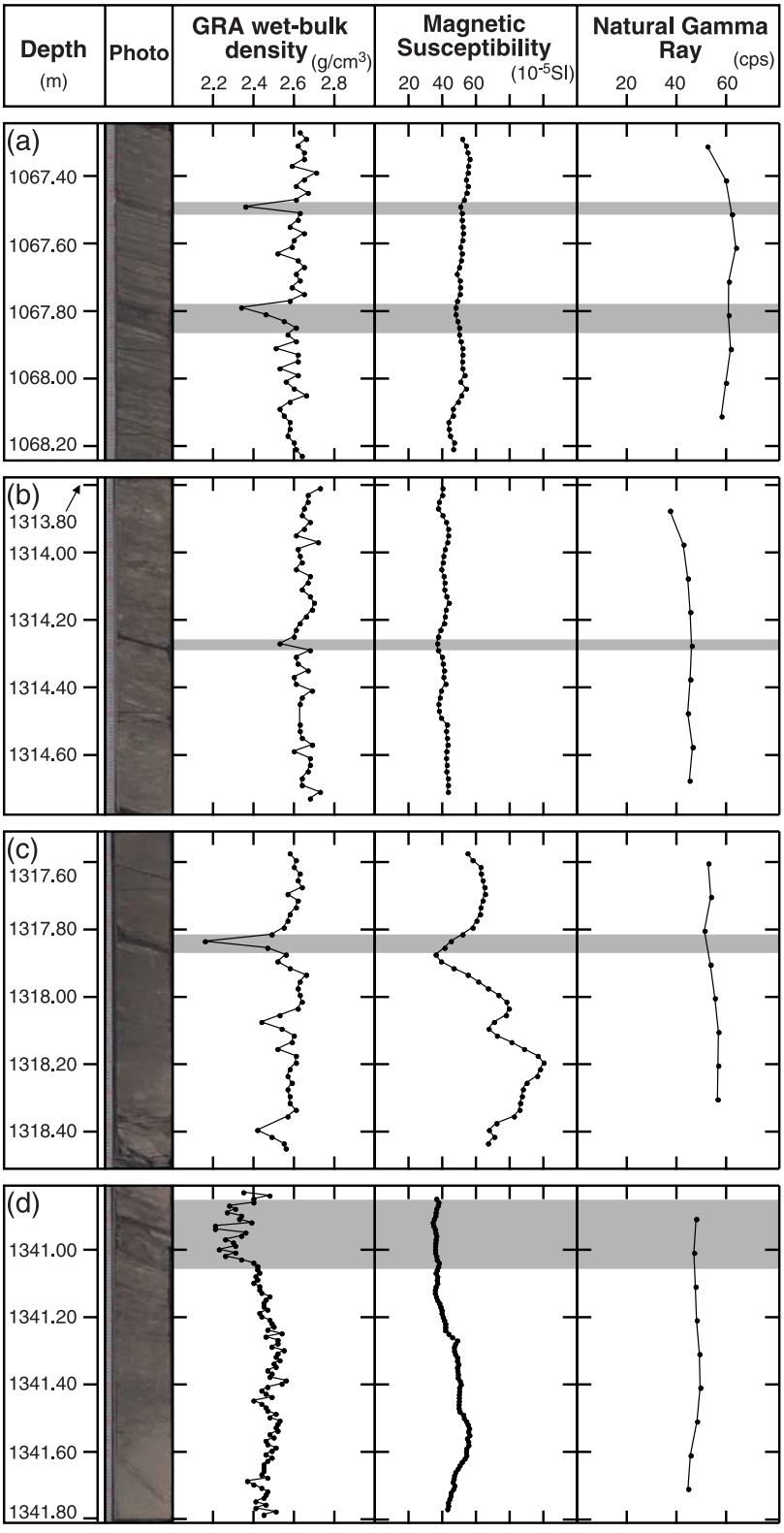

Figure 13. Density, magnetic susceptibility, and natural gamma ray radiation (NGR) logs from minor fault zones, along with photo images.

and breccia zones were fragile and subject to collapse at the outer edges, and some portions were frequently washed out. Consequently, the total analyzed volume of these portions of the sequence was less than that of other parts of the sequence. However, since the cross-sectional sediment thickness was measured with the MSCL to calibrate the density calculation, the lower densities recorded in the gouge and breccia zones are not likely to be artifacts resulting from sample collapse or washout.

[45] Rather, we attribute the lower GRA densities in the gouge zone to extensive microscale fracturing and cracks within the zone and/or to the loss of atoms with high atomic number. We were unable to detect obvious fractures and cracks in our mesoscopic observations, and a chemical analysis was not performed. Therefore we are unable to identify the cause rigorously but can conclude that the lower GRA densities within the black gouge zones are not artifacts. Moreover, lower GRA densities seem to coincide with lower X-ray attenuation on the X-ray CT images (Figures 6, 8, and 10).

7.2. High Magnetic Susceptibility Within the Three Major Fault Zones

[46] In the three major fault zones, high magnetic susceptibilities were recorded within the black gouge zones and the BM disks. Although magnetic susceptibility measurement is convenient and nondestructive, detailed rock magnetic and nonmagnetic analyses are required to examine the cause of high magnetic susceptibility because magnetic susceptibility is affected by various factors, such as the concentrations and kinds of magnetic minerals contained in the rocks, the grain size of the magnetic minerals, and sometimes the concentrations of paramagnetic (iron-bearing) and diamagnetic (iron-free) minerals [e.g., *Dearing*, 1999]. *Mishima et al.* [2006] conducted detailed rock magnetic analyses of the BM disks and surrounding rocks within FZB1194 and FZB1243. They suggested that the change in grain size of magnetic minerals did not account for the high magnetic susceptibility within the BM disks because decreases in the concentrations of very fine magnetic minerals could increase magnetic susceptibility [*Maher*, 1988]. Rather, they showed that magnetic minerals such as magnetite and maghemite had formed within the BM disks as a result of the thermal decomposition of paramagnetic minerals at temperature above 400°C and inferred that the formation of these minerals accounted for the increase in magnetic susceptibility.

[47] Decomposition of paramagnetic minerals and formation of magnetic minerals might also explain the high magnetic susceptibility within the black gouge zone in FZB1136. Samples from FZB1136 were subjected to magnetic hysteresis measurements [Mishima, personal communication, 2007], and the black gouge samples showed more hysteretic behavior and stronger magnetization in a low magnetic field than samples from the surrounding rocks, suggesting that the gouge samples had a higher ferromagnetic mineral content. In contrast, the rate of increase of magnetization in a high magnetic field was lower in the black gouge zone than in the surrounding rocks, implying that the gouge zone samples had a lower paramagnetic mineral content. Therefore decomposition of paramagnetic minerals and formation of magnetic minerals might have occurred not only within the BM disks in FZB1194 and FZB1243 but also within the black gouge zone in FZB1136.

[48] On the other hand, none of the minor fault zones showed high magnetic susceptibilities (Figure 13). Although detailed magnetic mineral analyses would be required to examine possible magnetic change within the minor fault zones, we presume that the temperature of these minor zones might not have reached a high enough level to form magnetic minerals. When this was the case, frictional heating to higher temperatures would generally accompany slip associated with a relatively high frictional coefficient on the fault plane. Given a constant frictional coefficient, the temperature reached as a result of frictional heating would depend on the slip velocity and displacement. The minor fault zones might not have been produced by slips with sufficient velocity or displacement to achieve a sufficiently high temperature to form magnetic minerals by frictional heating.

7.3. Relationship With the 1999 Chi-Chi Earthquake

[49] The plane or zone of slip during the 1999 Chi-Chi earthquake was not identified in this study. However, in the temperature measurements from hole A, *Kano et al.* [2006] observed a slight heat signal around FZA1111 (corresponding to FZB1136 in hole B) and concluded that the heat signal had been produced by frictional heating during the earthquake. *Ma et al.* [2006] found both a 12-cm-thick primary slip zone and a 2-cm-thick major slip zone within the shallowest fault zone in hole C (a sidetrack from hole B) and concluded that the major slip zone was associated with the 1999 earthquake. *Wu et al.* [2007] reported low seismic velocity, low electrical resistivity, and a major stress orientation anomaly around FZA1111 in geophysical logs from hole A, suggesting that the shallowest fault zone was most likely related to the 1999 Chi-Chi earthquake. Therefore the shallowest fault zone likely slipped during the 1999 earthquake.

[50] We found high magnetic susceptibilities within FZB1136, FZB1194, and FZB1243, which might have resulted from the formation of ferromagnetic magnetite or maghemite by thermal decomposition of paramagnetic minerals, possibly reflecting a thermal anomaly caused by frictional heating during an earthquake. The BM disks, identified as pseudotachylytes with a low degree of melting [*Hirono et al.*, 2006a], within both FZB1194 and FZB1243 are evidence for frictional heating in these major fault zones. The heat signal in FZA1111, reported by *Kano et al.* [2006], is strong evidence for frictional heating during the last earthquake. The significantly lower inorganic carbon content within the black gouge zone in FZB1136 [Ikehara et al., personal communication, 2007] and the BM disks in FZB1194 and FZB1243 [*Hirono et al.*, 2006a] than in the surrounding gray gouge zones or host rocks is another possible indication that these zones have been subjected to high temperature because thermal decomposition of carbonate minerals occurs at high temperatures above approximately 400°C [*Warne and French*, 1984]. Taking our results and those of previous reports into consideration, we suggest that all three major fault zones have experienced high temperatures at some time in the

past, probably induced by frictional heating during several repeated earthquakes.

[51] Next we discuss the mechanism of dynamic slip weakening during earthquake. Frictional melting and thermal pressurization are consistent with the reported evidence of frictional heating. However, elasto-hydrodynamic lubrication as a possible mechanism cannot be addressed here because its relationship with frictional heating is not well understood. All of the black gouge and gray gouge zones within FZB1136, FZB1194, and FZB1243 showed lower GRA densities, perhaps owing to extensive microscale fractures and cracks and/or the loss of the atoms with high atomic number. If the first explanation is correct, then the mechanism was more likely thermal pressurization than frictional melting because melting would be expected to produce relatively higher densities. Therefore if we assume that the low GRA densities and high magnetic susceptibilities can be associated with the 1999 earthquake, then thermal pressurization is the most likely faulting mechanism of that event. However, this hypothesis must be tested in further investigations, such as microscopic examination of fault zone rocks, to identify the slip plane or slip zone responsible for the most recent earthquake activity and thus to better understand the faulting mechanism of the 1999 Chi-Chi earthquake.

8. Summary

[52] Hole B of the TCDP penetrated the Chelungpu fault, and core samples were recovered from 948.42- to 1352.60-m depth. Three fault zones, FZB1136, FZB1194, and FZB1243, were recognized in the core samples as a series within the Chelungpu fault. We conducted nondestructive continuous physical property measurements on all core samples and found that the three major fault zones were characterized by lower GRA densities and higher magnetic susceptibilities. The lower GRA densities might have resulted from extensive fracturing and cracks within the fault zones and/or loss of atoms with high atomic number but do not likely reflect an artificial washout effect. The higher magnetic susceptibility values might have resulted from the formation of ferromagnetic magnetite or maghemite by thermal decomposition of paramagnetic minerals. This phenomenon is common in fault gouge that has been subjected to high temperature. *Enomoto and Zheng* [1998] and *Nakamura and Nagahama* [2001] reported high magnetic susceptibility in fault gouge within the Nojima fault caused by the production of new magnetite. On the other hand, core samples from some minor fault zones were characterized by lower GRA densities and no change in magnetic susceptibility or NGR emission. Magnetic susceptibility may thus be key to detection of frictional heating during an earthquake.

[53] Unfortunately, the fault zone, shear zone, or plane that slipped during the 1999 earthquake has still not been identified with certainty. Further investigations, such as microstructural examination, may provide additional information by which to identify the slip zone or plane, knowledge of which is important for gaining an understanding of the faulting mechanism acting within the fault zone system during the 1999 Chi-Chi earthquake.

[54] **Acknowledgments.** We thank James Evans and an anonymous reviewer for their many constructive comments, and we also thank Editor John Mutter and Associate Editor Isabelle Manighetti for editing this paper and giving valuable comments. This research was supported by the Ministry of Education, Science, Sports and Culture, Grant-in-Aid for Young Scientists 18740323, 2006.

References

Andrews, D. J. (2005), Thermal pressurization explains enhanced long-period motion in the Chi-Chi earthquake, *Eos Trans. AGU*, *86*(52), Fall Meet. Suppl., Abstract S34A-04.

Biegel, R. L., and C. G. Sammis (2004), Relating fault mechanics to fault zone structure, *Adv. Geophys.*, *47*, 65–111.

Brodsky, E., and H. Kanamori (2001), Elastohydrodynamic lubrication of faults, *J. Geophys. Res.*, *106*, 16,357–16,374.

Chen, K. C., B. S. Huang, J. H. Wang, W. G. Huang, T. M. Chang, R. D. Hwang, H. C. Chiu, and C. C. P. Tsai (2001), An observation of rupture pulses of the 20 September 1999 Chi-Chi, Taiwan, earthquake from near-field seismograms, *Bull. Seismol. Soc. Am.*, *91*, 1247–1254.

Chester, F. M., J. P. Evans, and R. L. Biegel (1993), Internal structure and weakening mechanisms of the San Andreas Fault, *J. Geophys. Res.*, *98*, 771–786.

Chung, J. K., and T. C. Shin (1999), Implications of the rupture process from the displacement distribution of strong ground motions recorded during the 21 September 1999 Chi-Chi, Taiwan earthquake, *Terr. Atmos. Ocean. Sci.*, *10*, 777–786.

Dearing, J. (1999), Magnetic susceptibility, in *Environmental magnetism: a practical guide*, edited by J. Walden, F. Oldfield, and J. Smith, pp. 243, Quaternary Research Association, London.

Enomoto, Y., and Z. Zheng (1998), Possible evidences of earthquake lightning accompanying the 1995 Kobe earthquake inferred from the Nojima fault gouge, *Geophys. Res. Lett.*, *25*, 2721–2724.

Hirono, T., M. Takahashi, and S. Nakashima (2003), Direct imaging of fluid flow in geomaterials by X-ray CT, *Geol. Soc. London, Spec. Publ.*, *215*, 107–115.

Hirono, T., et al. (2006a), Evidence of frictional melting within disk-shaped black materials discovered from the Taiwan Chelungpu fault system, *Geophys. Res. Lett.*, *33*, L19311, doi:10.1029/2006GL027329.

Hirono, T., et al. (2006b), High magnetic susceptibility of fault gouge within Taiwan Chelungpu fault: Nondestructive continuous measurements of physical and chemical properties in fault rocks recovered from Hole B, TCDP, *Geophys. Res. Lett.*, *33*, L15303, doi:10.1029/2006GL026133.

Kano, Y., J. Mori, R. Fujio, H. Ito, T. Yanagidani, S. Nakao, and K. Ma (2006), Heat signature on the Chelungpu fault associated with the 1999 Chi-Chi, Taiwan earthquake, *Geophys. Res. Lett.*, *33*, L14306, doi:10.1029/2006GL026733.

Kikuchi, M., Y. Yagi, and Y. Yamanaka (2000), Source process of the Chi-Chi, Taiwan, earthquake of September 21, 1999 inferred from teleseismic body waves, *Bull. Earthquake Res. Inst., Univ. Tokyo*, *75*, 1–13.

Lee, Y., M. Hsieh, S. Lu, T. Shih, W. Wu, Y. Sugiyama, T. Azuma, and Y. Kariya (2003), Slip vectors of the surface rupture of the 1999 Chi-Chi earthquake, western Taiwan, *J. Struct. Geol.*, *25*, 1917–1931.

Ma, K. F., C. T. Lee, Y. B. Tsai, T. C. Shin, and J. Mori (1999), The Chi-Chi Taiwan earthquake: Large surface displacements on inland thrust fault, *EOS*, *80*, 605–611.

Ma, K. F., T. R. Song, S. J. Lee, and S. I. Wu (2000), Spatial slip distribution of the September 20, 1999, Chi-Chi Taiwan earthquake: Inverted from teleseismic data, *Geophys. Res. Lett.*, *27*, 3417–3420.

Ma, K. F., E. E. Brodsky, J. Mori, C. J. T. R. A. Song, and H. Kanamori (2003), Evidence for fault lubrication during the 1999 Chi-Chi, Taiwan, earthquake (Mw7.6), *Geophys. Res. Lett.*, *30*(5), 1244, doi:10.1029/2002GL015380.

Ma, K. F., et al. (2006), Slip zone and energetics of a large earthquake from the Taiwan Chelungpu-fault Drilling Project, *Nature*, *444*, 473–476.

Maher, B. A. (1988), Magnetic properties of some synthetic sub-micron magnetites, *Geophys. J.*, *94*, 83–96.

Mishima, T., T. Hirono, W. Soh, M. Ikehara, W. Lin, W. Tanikawa, E. Yeh, S. Song, and C. Wang (2006), Thermal history estimation of the Taiwan Chelungpu Fault using rock-magnetic methods, *Geophys. Res. Lett.*, *33*, L23311, doi:10.1029/2006GL028088.

Nakamura, N., and H. Nagahama (2001), Changes in magnetic and fractal properties of fractured the Nojima Fault, Japan, *Isl. Arc*, *10*, 486–494.

Schulz, S. E., and J. P. Evans (1998), Spatial variability in microscopic deformation and composition of the Punchbowl fault, southern California: implications for mechanisms, fluid-rock interaction, and fault morphology, *Tectonophysics*, *295*, 223–244.

Shin, T. C., K. W. Kuo, W. H. K. Lee, T. L. Teng, and Y. B. Tsai (2000), A preliminary report on the 1999 Chi-Chi (Taiwan) earthquake, *Seismol. Res. Lett.*, *71*, 24–30.

Sibson, R. H. (1977), Fault rocks and fault mechanisms, *J. Geol. Soc. (London)*, *133*, 191–213.

Sone, H., E. Yeh, T. Nakaya, J. Hung, K. Ma, C. Wang, S. Song, and T. Shimamoto (2007), Mesoscopic structural observations of cores from the Chelungpu fault system, Taiwan-Chelungpu-fault Drilling Project Hole-A, Taiwan, *Terr. Atmos. Ocean. Sci.*, in press.

Wang, C., C. Chang, and H. Yen (2000), An interpretation of the 1999 Chi-Chi earthquake in Taiwan based on the thin-skinned thrust model, *Terr. Atmos. Ocean. Sci.*, *11*, 603–630.

Wang, C., C. Li, and H. Yen (2002), Mapping the northern portion of the Chelungpu fault, Taiwan by shallow reflection seismics, *Geophys. Res. Lett.*, *29*(16), 1790, doi:10.1029/2001GL014496.

Warne, S. St. J., and D. H. French (1984), The decomposition of anhydrous carbonate minerals in coal and oil shale ashes produced at temperatures of 400 and 575°C, *Thermochim. Acta*, *75*, 139–149.

Wu, H., K. Ma, M. Zoback, N. Boness, H. Ito, J. Hung, and S. Hickman (2007), Stress orientations of Taiwan Chelungpu-Fault Drilling Project (TCDP) hole-A as observed from geophysical logs, *Geophys. Res. Lett.*, *34*, L01303, doi:10.1029/2006GL028050.

Yeh, E., et al. (2007), Preliminary results of core description from the Hole-A of the Taiwan Chelungpu-fault Drilling Project, *Terr. Atmos. Ocean. Sci.*, in press.

Yue, L., J. Suppe, and J. Hung (2005), Structural geology of a classic thrust belt earthquake: The 1999 Chi-Chi earthquake Taiwan (M_w = 7.6), *J. Struct. Geol.*, *27*, 2058–2083.

K. Aoike and H. Ito, Center for Deep Earth Exploration, Japan Agency for Marine-Earth Science and Technology, Yokohama, Japan.

T. Fujiki, T. Kondo, T. Kuramoto, L. Maeda, S. Moriya, H. Muraki, M. Nishimura, T. Tanaka, T. Sugawara, and K. Sugiyama, Marine Works Japan Ltd., Yokohama, Japan.

Y. Hashimoto, Department of Natural Environmental Science, Faculty of Science, Kochi University, Kochi, Japan.

T. Hirono, Nakashima-Lab., Department of Earth and Space Science, Graduate School of Science, Osaka University, Toyonaka 560-0043, Osaka, Japan. (hirono@ess.sci.osaka-u.ac.jp)

J.-H. Hung, K.-F. Ma, Y.-B. Tsai, and C.-Y. Wang, Institute of Geophysics, National Central University, Jhongli, Taiwan.

M. Kinoshita, Institute for Research on Earth Evolution, Japan Agency for Marine-Earth Science and Technology, Yokosuka, Japan.

W. Lin and W. Soh, Kochi Institute for Core Sample Research, Japan Agency for Marine-Earth Science and Technology, Nankoku, Kochi, Japan.

O. Matsubayashi, Institute for Geo-Resources and Environment, National Institute of Advanced Industrial Science and Technology, Tsukuba, Japan.

T. Mishima and M. Murayama, Center for Advanced Marine Core Research, Kochi University, Nankoku, Kochi, Japan.

H. Sone, Department of Geophysics, School of Earth Sciences, Stanford University, Stanford, CA, USA.

S.-R. Song and E.-C. Yeh, Department of Geosciences, National Taiwan University, Taipei, Taiwan.